*Geosciences and Engineering, Vol. 8, No. 13 (2020), pp. 167–184.*

# CT BASED ANALYSIS OF PORE NETWORK OF RESERVOIR ROCKS

HASAN ATRASH – FELICITÁSZ VELLEDITS

*Institute of Mineralogy and Geology, University of Miskolc*
*e-mail: hasan.alatrash87@gmail.com*

**Abstract:** High-resolution X-ray Computed Tomography (CT) is a novel technique suited to a wide range of geological investigations. It is a quick and non-destructive method to produce images that correspond closely to serial sections through an object. Sequential contiguous images are compiled to create three-dimensional representations that can be manipulated digitally to perform efficiently a large array of measurements and visualizations. In this study we combined conventional core analysis technique with micro-scale Computed Tomography imaging technique to extract pore network properties of carbonate rocks. In order to detect pore properties from the CT images different filtering algorithms and various segmentation techniques were applied to obtain robust data, which were compared with those of mercury injection texts carried out in the laboratory on the same samples. The methodology is applied to a set of real porous media and the resulting pore network statistics showed great variability compared to lab results due to limitations in voxel resolution. Despite this, useful information about the pore constituents could be extracted.

***Keywords:*** *micro-CT, image processing, image segmentation, pore structure characterization*

## 1. INTRODUCTION

Understanding the flow in the porous media requires the knowledge of the pore structure properties. A reservoir rock is most often characterized by its porosity and in particular by how its pores are distributed and how they are in connection with each other. For this reason, many efforts have been made to characterize the internal structure of porous media, one of which is the use of Computer Tomography (CT). In recent years, significant progress has been made in the development of high-resolution 3D tomographic imaging and registration techniques to directly image rock microstructures across a continuous range of length scales. This emerging new technology provides a direct characterization of multi-modal pore size distributions and allows us to predict flow properties and the productivity of a complex reservoir [1]. In our experiment a combination of conventional lab poro-perm measurement was combined with high-resolution X-ray computed tomography. Measurements were conducted on two samples extracted from two cores taken from a carbonate oil reservoir. Conventional methods were applied to calculate porosity and permeability including MICP (mercury injection capillary pressure), while an industrial micro-CT analysis was applied in order to get a 3D pore structure characterization. Three main objectives have been defined for the μ-CT study:

– 3D visualization and understanding of the variability of the pore structure and the related pore network;
– optimization of the selected core plugs for upcoming conventional core analysis and a later comparison of the measured conventional core analysis results with the direct calculation of petrophysical properties;
– investigation and characterization of rock pore network properties and how it relates to petrographic parameters in 3D.

## 2. SAMPLES AND METHODS

The work flow applied for each sample is outlined in *Figure 1*. It is based on sample preparation, experimental imaging and image quality control, and pore network characterization, and the results are compared with those of conventional core analyses.

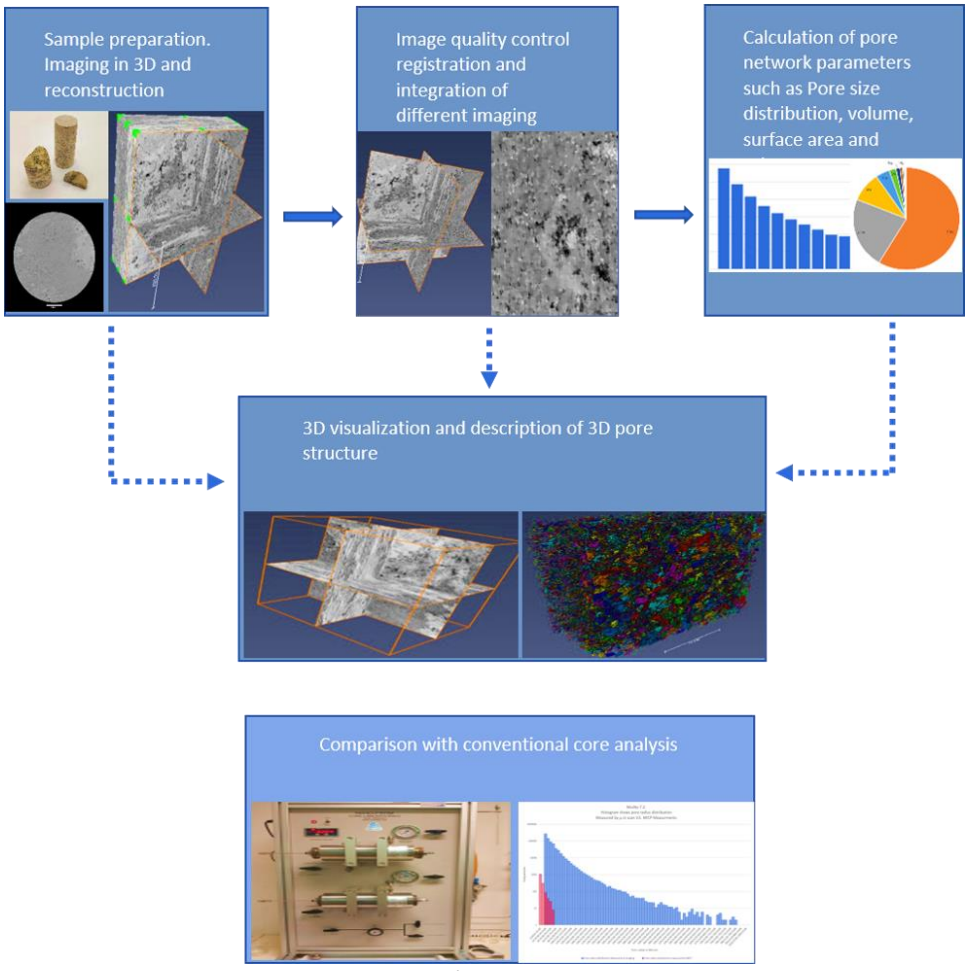


***Figure 1***
*Work flow undertaken for digital core analysis*

### 2.1. X-ray micro-CT imaging

X-ray Computed Tomography (CT) is a non-destructive tool used widely in geoscience for research purposes. It can be used for making three-dimensional reconstruction of the variation of attenuation coefficient "μ" passed through the object of study, as expressed in Beer's law:

$$I = I_0 \exp(-\mu x), \tag{1}$$

where I is the attenuated intensity after the X-rays have passed through an object of thickness x, $I_0$ is the incident radiation intensity, and μ is the linear attenuation coefficient [2].

The data obtained from this technique is digitized, making it suitable for quantitative analysis. The basic principle of X-ray CT lies in X-ray radiography. The main components are an X-ray source, an object that is irradiated and a detector that measures the attenuated X-rays. As a result, radiograph is produced. Unlike the two-dimensional radiographs, which cause a loss of depth information X-ray computed tomography, provides a complete 3D reconstruction of the original structure of the sample, which enables the rock grains and pores to be distinguished [3, 4]. The working principle of CT scanners is schematically depicted in *Figure 2*. X-Ray attenuation is the reduction of intensity of the X-ray beam when it passes through the subject. Energy scattering and absorption are the main reasons for the attenuation of the X-ray beam and it can be affected by many factors like atomic number, density of the absorber, and beam energy. The denser the object or the higher the atomic number is, the more the X-rays are attenuated. It is possible to reconstruct this internal information from X-rays that have traveled different paths through the sample [5]. The generated X-rays are attenuated by the components of the sample and captured by the detector, generating projection images. Then these images are reconstructed by mathematical process by the use of a computer attached to the machine. The final three-dimensional images acquired by the CT-scan proceed from a stacking sequence of two-dimensional slice images. These two-dimensional images resulted from a large number of projection images attained by the scanning system. Then the inversion process takes place to produce the special images from projections, employing the filter-back projection algorithm. This algorithm is adapted to cone geometry and consists of two steps, filtering the projection and back projecting the information on the three-dimensional image volume that represents the scanned sample. The reconstruction software used at the University of Miskolc is VG Studio Max 3.1. At the end of the reconstruction stage a stack of two-dimensional slices are produced and ready for visualization and further analysis. 3D images of the small plugs at ~35 mm in diameter are imaged. The tomogram images were obtained using a μ-CT at the University of Miskolc at a voxel size down to ~20 μm resolution.

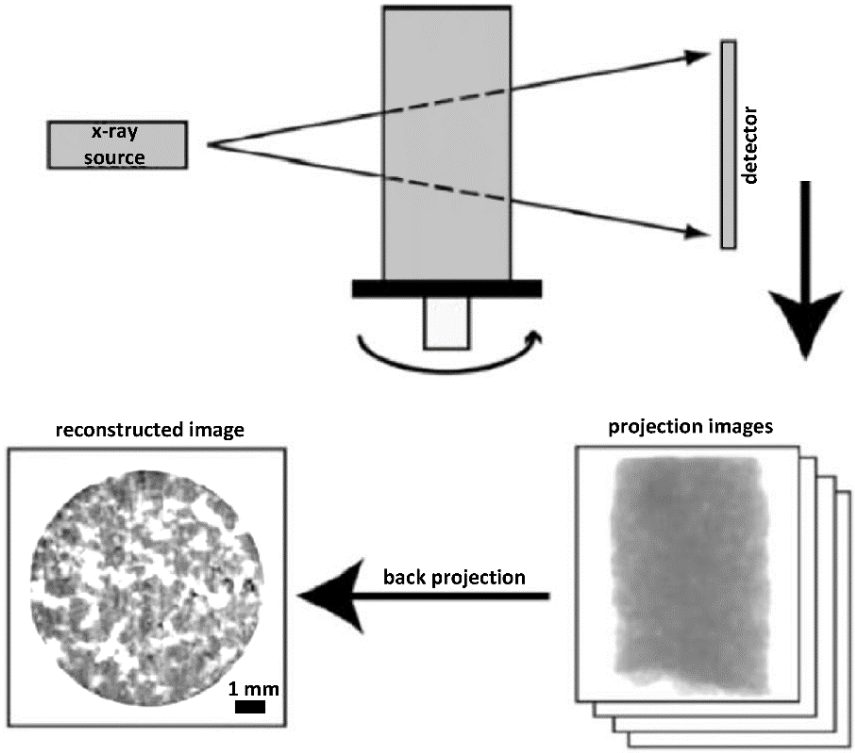


***Figure 2***

*Working principle of CT scanners. The X-rays are generated in the source, travel through the object where they are attenuated, and are then captured by the detector. From* [6]

### 2.2. Mercury injection capillary pressure (MICP)

Mercury injection examines the distribution of pressure-volume relationships regulating the entry of a non-wetting phase (mercury) into a pore system. Capillary forces control the entry of mercury into the pores. Mercury intrusion can only progress when increasing pressure overcomes these forces. The accepted view of this procedure is that MICP detects a sequence of pore throats. Converting the pressure values to pore size using the Washburn equation models the pore system as a series of interconnected, cylindrical tubes *(Equation 2)*. Therefore, the MICP pore length is the area equivalent diameter of a circle and consequently provides no information about either the vector length or the aspect of the pore system

$$\text{Pore diameter} = \frac{4\gamma c \cdot \cos\theta}{Pc}, \tag{2}$$

where c= Washburn constant, Pc= Capillary pressure, γ= surface tension constant at 480dynes/cm, θ =contact angle through the wetting fluid (140°).

## 2.3. Image analysis

### *2.3.1. Phase identification and image quality enhancement*

The tomographic image is a reconstruction of the linear x-ray attenuation coefficient values, each corresponding to a voxel of the sample. Different phases (pore, mineral grains, and clays) have different attenuation values and may be distinguishable within the 3D data [7]. Still, in every obtained CT image there is a certain amount of noise and/or artifacts which decreases the quality of image segmentation results. *Figure 3* shows the effect of noise presented in the image on the binarization results. If feature extraction algorithms like region of interest operators are applied or image segmentation takes place, many of the features to be found will be expressing image noise only, for instance small edge elements [8]. To avoid these annoying effects which affect image quality, a filtering process has to be applied to the original digital image. Then another problem arises, which is that the smoothing of the image has to be achieved without blurring out the features of the image, especially when studying pore characteristics, where preserving the edges and corners with respect to their geometrical shape and magnitude is crucial. Existing smoothing algorithms are low pass and edge-preserving filters. Low pass filters have an effect on the image of smoothings features by rounding off the corners and blurring out small features which means image structures are geometrically damaged and thus this technique is not suitable for pore network extraction because the geometry of the pores will differ from the real values [8]. On the other hand, with edge-preserving filters such as edge-preserving smoothing filter provided by Avizo software and median filter these nonlinear algorithms calculate the filtered gray value taking into account the content of a defined neighborhood. The average of the voxels gray values is taken from the list of neighborhood voxels which have similar gray values, which makes it suitable for studying small features such as pore shape and sizes. It is noteworthy that image enhancement can have a great influence on segmentation results, and a detailed investigation of the effect of different filtering methods is of interest [9], but it was not the objective of this study.

Each edge-preserving filter has its own specific algorithm, but they all have in common the feature that all of them preserve edges. The edge-preserving-smoothing algorithm provided by Avizo software adopted for this study as it has shown good results compared to other applied smoothing algorithms such as median, Gaussian, and bilateral filters. While, the edge-preserving-smoothing algorithm is able to preserve the edges of the small features within the images and blurring of these features to a certain level is avoided [8]. The edge-preserving-smoothing algorithm models the physical process of diffusion. Similar to the Gaussian filter, it smooths out the difference between gray levels of neighboring voxels. This can be interpreted as a diffusion process in which energy between voxels of high and low energy (gray value) is leveled. In contrast with the Gaussian filter, it does not smear out the edges because the diffusion is reduced or stopped in the vicinity of edges. Thus, edges are preserved. This filter implements the non-linear diffusion algorithm [10].

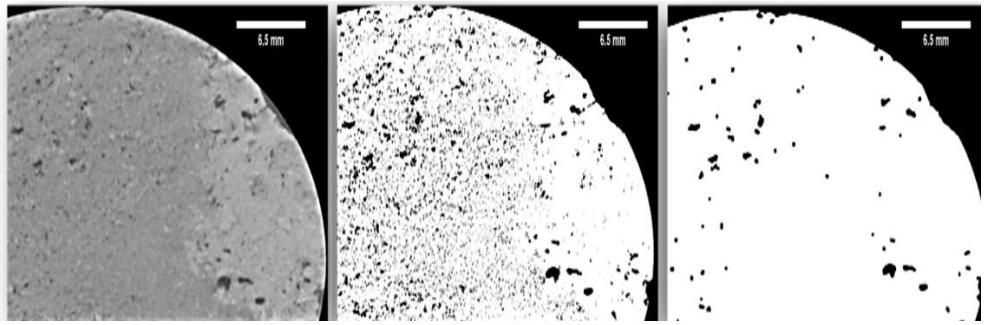


***Figure 3***

*Segmentation of noisy CT images against noise-free image. Corresponding 2-D slices from 3-D processing are shown. From left to right: original gray scale image, binary image obtained from a noisy image, and binary image obtained after filtering.*

### *2.3.2. Image segmentation*

Image segmentation is a crucial step in the process of differentiating the pore space from the matrix. During this step it will be determined whether each voxel in the image belongs to pore space or to the matrix; in other words, it creates segments of connected voxels based on some similarity criteria: intensity, color, texture, histogram, or features. There are various classification schemes for image segmentation methods proposed in literature [11, 12]. Since the information about pore shapes and sizes, and the solid matrix structure is not available prior to segmentation, texture or shape-based methods are inapplicable for segmentation of pore space and phase distribution in geomaterials, and are thus neglected in this study. The watershed method was not considered in this study either, because its applicability is generally limited to object detection in well-defined data or/and has already been binarized. Global thresholding is the most commonly applied approach. A single gray scale value is defined to separate regions of interest on the basis of analysis of the image histogram, as in *Figure 4*. Global thresholding methods may be divided into a number of subcategories based on the applied approach to select the optimal gray scale threshold. These include methods based on correlation between background and foreground pixel entropy analysis of the histogram shape, the similarity of attributes between the gray scale and binarized image or higher-order probability distributions, and spatial correlations between image pixels [11, 12]. Pores and grains can be segmented in the 3D image, which allows us to obtain statistics on the image data. Quantities associated with pore geometry, including size distributions, shape, volume, and connectivity, can also be derived from image data.

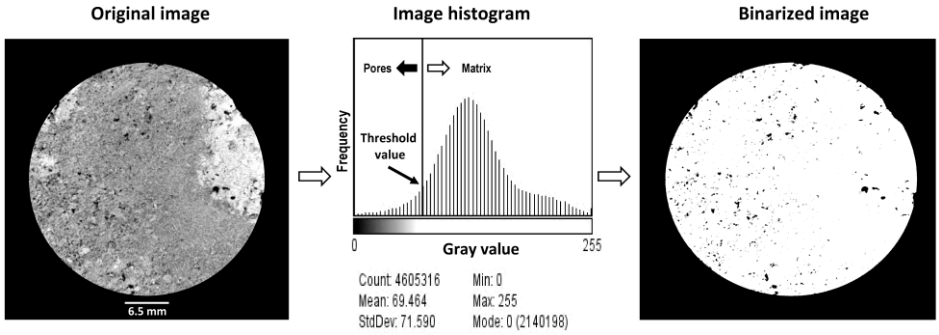


***Figure 4.***
*Histogram based binarization example corresponding to a 2-D slice throw. Well 4-3.2 sample.*

### *2.3.3. Porosity and pore parameter extraction*

Analysis of porosity by X-ray microtomography was carried out on two samples of carbonate rocks taken from a single well from two different depths and had similar petrophysical properties. The sample description is listed in *Table 1*. The resulting spatial resolution of the tomography images was 20 μm, which does not allow good classification of the pores nor a good reproduction of the internal porous space structure. Still some useful information could be extracted. Pore size distribution could be measured from the segmented image stacks. The pore size in 3-D was calculated as the equivalent diameter of a sphere of the same volume:

$$\mathrm{EqD} = \sqrt[3]{\frac{6\times\mathrm{volume}}{\pi}}\,. \tag{3}$$

Pore connectivity could not be detected due to the fact that the majority of pore throats sizes connecting the pores are lower than the image resolution as it was confirmed later by MICP measurement; consequently, pore connectivity was not included in this study.

Moreover, three perpendicular 2-D slices through one sample were randomly selected. The pore size distribution within each slice was measured and compared to the others. The reason for this is to find out whether the pore size distribution forms any particular pattern. The directions of the selected 2D slices or sections are one horizontal section through xy plane and the two other sections are perpendicular to the horizontal section and to each other through the xz plane and yz plane.

## 2.4. Investigated samples

The plugs we used were taken from a well core which was drilled in SW Hungary. The depth of the samples are 1967-m and 1966-m, and the samples IDs are Well 4-7.2 and Well 4-7.3, respectively. The well is situated in the Mid-Hungarian Mega-Unit, on the northern part of the Somogy Dráva-Valley basin, on the eastern part of

the Letenye-Mernye trough shown in *Figure 5*. According to a sedimentological study [13], the upper part of the Sarmatian limestone was deposited in a shallow marine environment whereas diagenesis happened in the meteoric zone around the sea level.

Two cylindrical core plugs were taken from the cores with a diameter of 35 mm for both samples for a μ-CT scan (see *Table 1* for core descriptions). The main criterion for selection of the samples aside from lithofacies is that they cover the range of the observed porosity and permeability for the cored interval. The samples have a porosity range of 25% to 28% and permeability of 30 mD to 55 mD based on laboratory measurements. Both of our samples were scanned by the micro CT facility at the University of Miskolc. To avoid artifacts occurring on the edges of the scanned samples, sub-volume cubes were extracted for segmentation and further analysis. The dimensions of the extracted cubes are 25 mm × 24 mm × 15 mm for Well.4-7.2 and 35mm × 24 mm × 12 mm for Well.4-7.3.


***Figure 5***
*Location map of the study area*

***Table 1***
*Sample description*

| Sample ID | Interval | Lithology | Lithology | Porosity measured by MICP |
|---|---|---|---|---|
| Well.4-7.2 | 1966.72m–1967m | limestone | In micritic matrix, calcareous algae and foraminifers occur | 28% |
| Well.4-7.3 | 1965.91m–1966m | limestone | In micritic matrix, calcareous algae and foraminifers occur | 22% |

## 3. RESULTS

### 3.1. Pore types and cement

The primary isolated intraparticle pores in the fossil shells remained partly empty during diagenesis *(Figures 6b, d)*. In the vadose zone due to infiltration of fresh undersaturated water intensive dissolution happened creating moldic *(Figure 6a)*

interparticle *(Figure 6d)* and vuggy pores. Not only was the majority of the matrix dissolved, but parts of bio- and intraclasts as well. Diagenesis continued in the phreatic zone when bladed calcite cement precipitated on the internal edge of the bioclasts *(Figure 6a)* and on the margin of the pores *(Figure 6c)*. After formation of the first cement generation diagenesis stopped. Thus, the majority of the primary and secondary pores provided sufficient space for the intruding hydrocarbon.

It is worth mentioning that distinguishing the different pore types that had been identified by microscopic investigation was not possible with the CT-images because the diameter of the scanned samples was about 3.5 cm and the associated voxel size resulting from this scan was 20 μm.

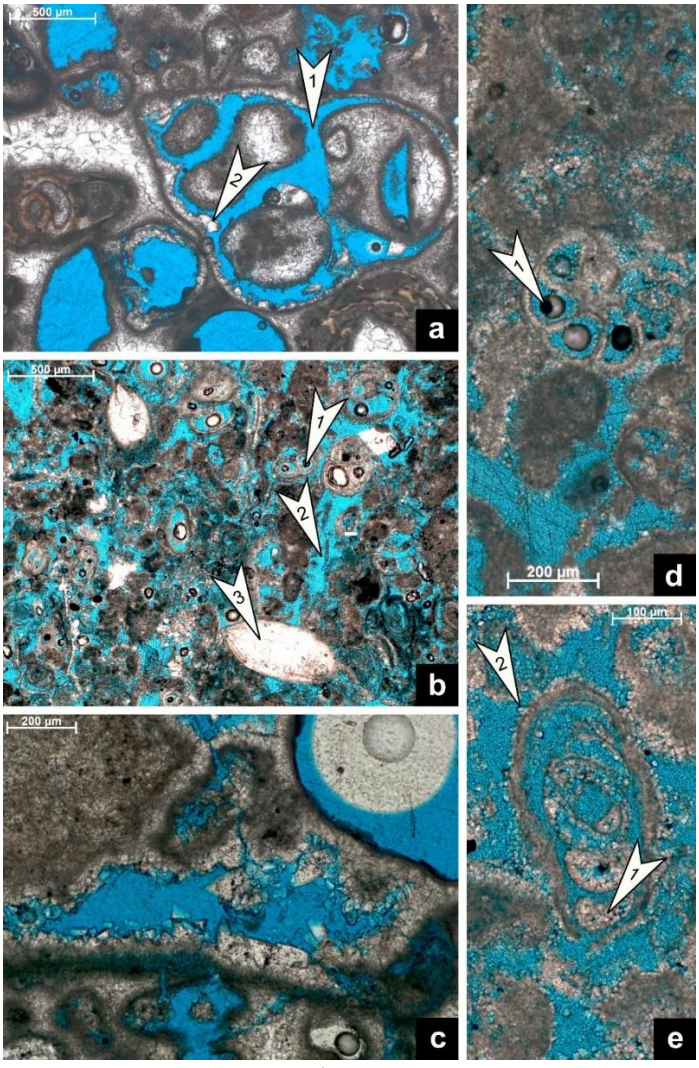


***Figure 6***

a. *Moldic porosity. The shell of a gastropod was totally dissolved creating moldic porosity (arrow 1). In the meteoric phreatic zone bladed cement crystals precipitated on the internal wall of the moldic pore (arrow 2). Well.4-7.3 1966 m, horizontal thin section.*
b. *Intra- and interparticle pores. The primary pores within the fossils remained empty (primary pores: arrow 1), and during meteoritic diagenesis the majority of the matrix was dissolved creating secondary intergranular pores (arrow 2). Note that shells of the ostracods were not separated after the death of the animal and were later filled by calcite (arrow 3). Well.4-7.2 1967 m vertical thin section.*
c. *Dog tooth cement. On the edge of the pore bladed calcite cements precipitated in freshwater phreatic zone. Well.4-7.3 1966 m. Horizontal thin section.*
d. *Intra-and interparticle porosity. The internal part of the foraminifera chambers remains empty, forming primary porosity (arrow 1). During diagenesis much of the matrix was dissolved by secondary intergranular pores being created. Well.4-7.2 1967 m horizontal thin section.*
e. *During diagenesis the original chambers of the foraminifera were partly filled by calcite cement (arrow 1). On the outer part of the shell bladed calcite cements were precipitated in the fresh water phreatic zone (arrow 2). The bio and intraclasts were partly dissolved and on their outer parts bladed cement precipitated. Well.4-7.2 1967 m, vertical thin section.*

### 3.2. Pre-processing

The images from the scan exhibit some noise. For this reason, we used noise reduction filters. After applying different smoothing filters such as median, Gaussian, bilateral and edge preserving smoothing filters the final filter was adopted for the whole data set by Avizo software. The edge preserving filter has produced good results with regards to preserving pore shapes and edges compared to the other filters. The conserving effect for important image structures is illustrated in *Figure 7*. The figure shows the effect of median and edge preserving smoothing filters. Some small pores were blurred out after applying the median filter, while they were preserved when applying the edge preserving smoothing filter. *Figure 8* compares the effect of these two filters on a gray value edge with the original image using the Lineprobe tool provided by Avizo software. This tool allows us to inspect the gray values along a line placed in the region of interest, see *Figure 8a*, for illustration. The gray value was measured along one pore in the original image without filtering and after filtering. The results are plotted in *Figure 8b*, and it is clear that the gray values of the pore edges in the image filtered by the edge preserving filter almost match those in the original image, unlike the median filter, where the gray values of the edges are modified to lower values, which can lead to blurring of the edges.

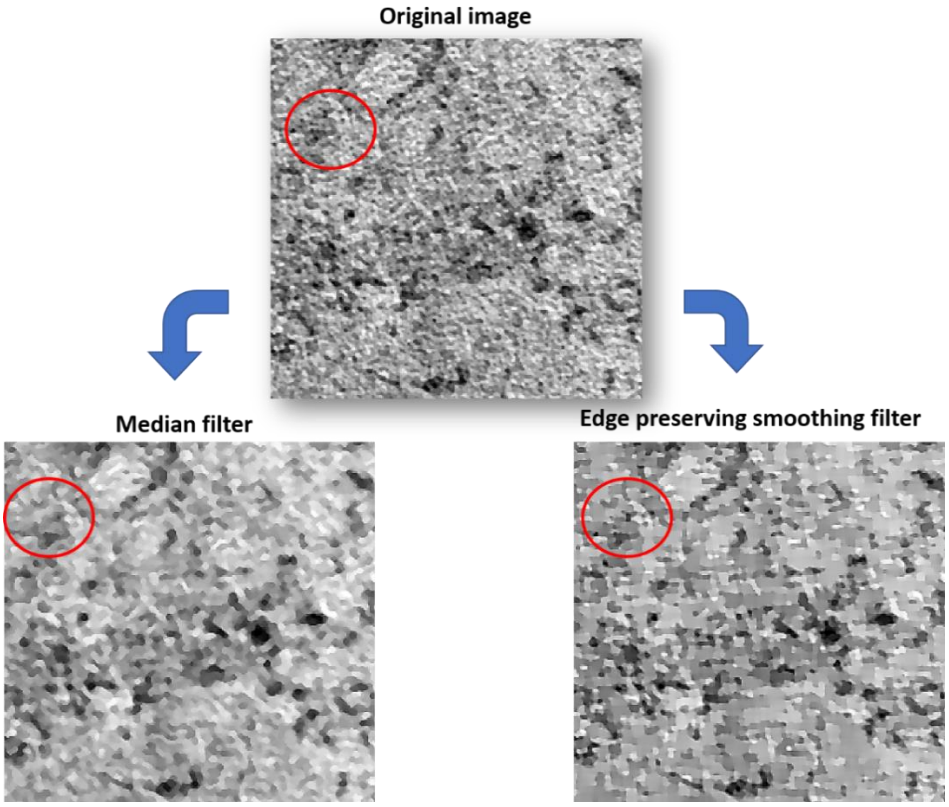


***Figure 7***
*Resulting images after application of different smoothing filters*

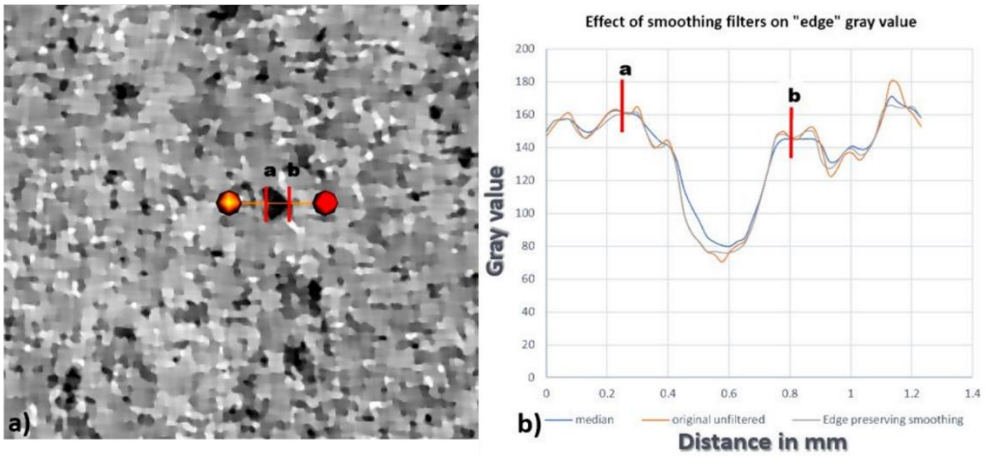


***Figure 8***
*Effect of smoothing filtering on "edge" gray value: a) is an illustration of the lineprobe tool, a) and b) mark the edges of the pore in both figures*

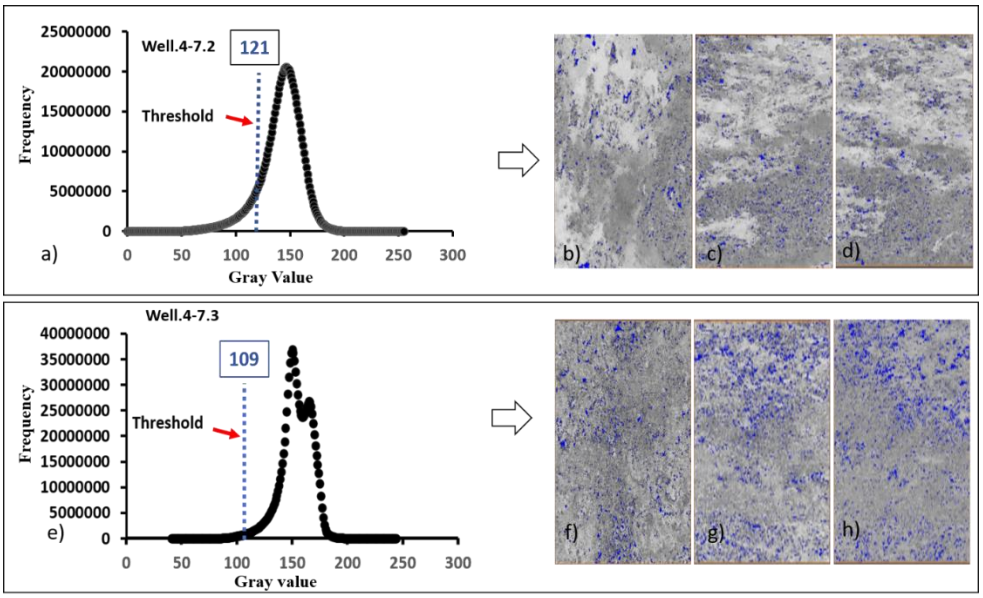


***Figure 9***

*Selected threshold value based on histogram readings for both samples where a) is the histogram for gray values distribution for sample Well.4-7.2 and b) c) and d) tomograms in (xy) (yz) (xz) sections; e) to h) demonstrate the same for sample Well.4-7.3. Pores are highlighted in blue.*

### 3.3. Post processing image segmentation and binarization

The segmentation process was performed to capture the geometry of the samples for quantitative analysis. In most studies the segmentation process is conducted by selecting a threshold, with gray scale values below a certain threshold value assigned to one phase and the gray scale values above the threshold values assigned to the other phase. Our samples consist of two constituents, pores and matrix. Each sample with the size of 1240 × 1150 × 750 pixels was extracted for segmentation and further analysis. The gray scale ranges from 0 to 255 for both samples and the global threshold values for pore constituents for well.4-7.2 and well.4-7.3 samples is 121 and 109 respectively. The accuracy of the segmentation process should be roughly evaluated by selecting the threshold value and comparing the original gray scale image and the segmented image. In *Figure 9* the histogram of gray values was divided into two segments where the horizontal stage before the peak is segmented as the pore constituent, the peak and the horizontal stage after segmentation as the matrix. The pore constituents are well segmented in three orthogonal planes "xy-xz-yz" where the pores are highlighted in blue. The distribution curve validates the success of segmentation process to some extent. Following the segmentation and evaluation process of Well.4-7.2 the other sample was also segmented.

### 3.4. Porosity and pore size distribution (PSD)

A three-Dimensional representation of the segmented pore constituent is shown in *Figure 10*, and a summary of the segmented tomograms is listed in *Table 2*. In *Figure 10* pores with a size ≥ 500 µm are labeled with different colors, while the rest of the pores appear in light blue. Furthermore, the heterogeneity of the samples in different directions was also evaluated by calculating the pore diameter within three orthogonal sections (xz-yz-xy). For both samples, there is homogeneity in yz plane and xz plane, while it differs in xy plane as shown in *Figure 11*. This can be attributed to the infiltration of undersaturated water during vadose diagenesis coming from the upper layers and creating pathways in the vertical direction.

*Table 2*

*Summary of the segmented tomograms*

| Sample ID | Sample geometry | Number of 2-D slices | Voxel size | Segmented-cube geometry | Total number of pores |
|---|---|---|---|---|---|
| Well.4-7.2 | 3.5 cm × 3.4 cm | 700 | 20 µm | 30 mm × 24 mm × 14 mm | ~700,000 |
| Well.4-7.3 | 3.5 cm × 3.1 cm | 600 | 20 µm | 30 mm × 24 mm × 12 mm | ~610,000 |

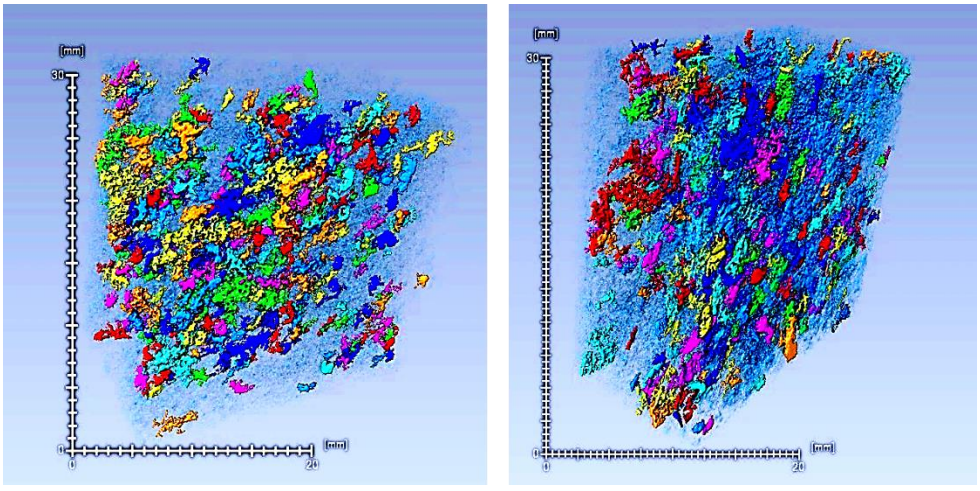

***Figure 10***

Segmen*ted pore constituent at 20 µm resolution in volume rendering for both samples: Well.4-7.2 sample (left) and Well.4-7.3 sample (right); pores with a size ≤ 500 µm depicted in light blue, all other colors refer to pores ≥ 500 µm*

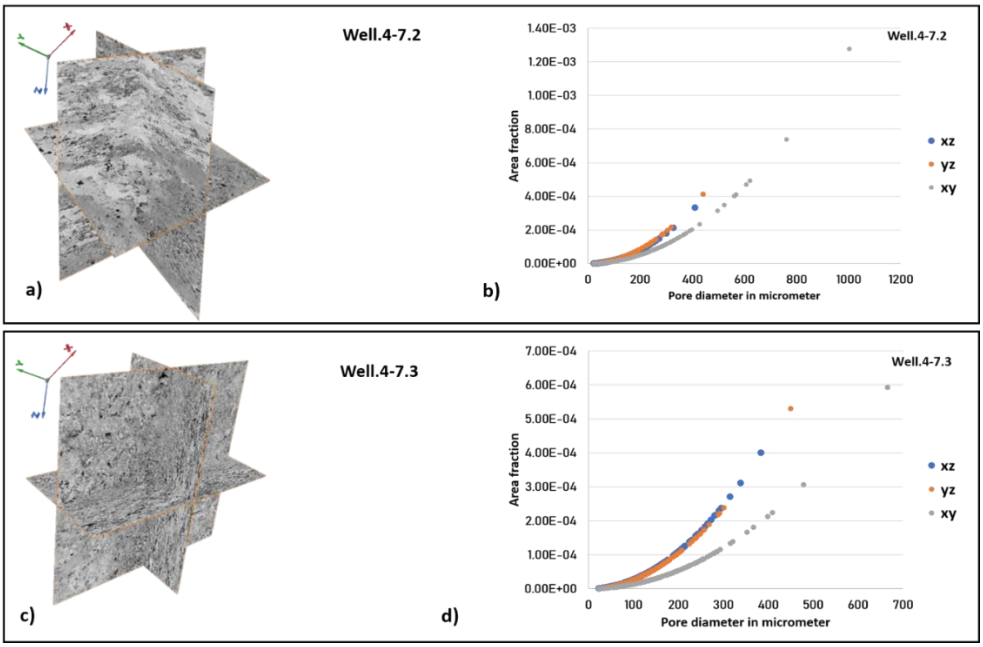


***Figure 11***

*a) Three orthogonal sections through Well.4-7.2 sample, b) comparison of the plane fraction of the pore constituent in three orthogonal planes c) Three orthogonal sections of Well.4-7.3 sample, d) comparison plane fraction of the pore constituent in three orthogonal planes*

The PSD of the two samples was calculated, and the results are plotted in *Figure 12*. The PSD of the samples is uniformly distributed, and the pore size is within the range of 26 μm –1.5 mm with an average value at around 50 μm.

*Figures 11* and *12* demonstrate that the small pores are dominant in the samples and big pores are very few compared to the small ones. The resolution of tomograms resulting from μ-CT measurements was 20 μm therefore, small pores below this resolution could not be measured. Small plugs were also taken from the same samples for MICP measurement. The maximal mercury intrusion pressure of the MICP experiments was 392 MPa, corresponding to a minimum pore radius of 2 nm. The PSD measured by MICP ranges from 2 nm up to 55 μm with an average value of 15 μm. The PSD by μ-CT is continuous and has wider distribution than the PSD by the MICP experiment and covers a wide range of pore size, while the PSD by MICP covers a limited range. Considering Well.4-7.2 as an example, the peak of the PSD by μ-CT consists of a peak similar to the peak of the PSD by MICP; moreover, the frequency trend of the PSD by the two methods is similar. For the other sample, comparative results of PSD curves by μ-CT and MICP are similar to that of Well.4-7.2. It is noteworthy that, the PSD curves measured by different experiments were in good agreement only within a small interval between 25 μm and 55 μm. *Figure 13*

shows the similarity of the overlapping interval in between CT-PSD and those from MICP in q-q plots. Possible reasons for the differences in the PSD curves produced by μ-CT and MICP are as follows: (1) The PSD by μ-CT corresponds to the PSD of both connected pores and isolated pores, while MICP is restricted to connected pores; (2) the large pore radius calculated by MICP is based on the bundle-of-tubes model, and may be underestimated due to the shielding effects of the small pores. In any case, the PSD curves obtained from μ-CT analysis provide some useful information about the pore structure of the samples.

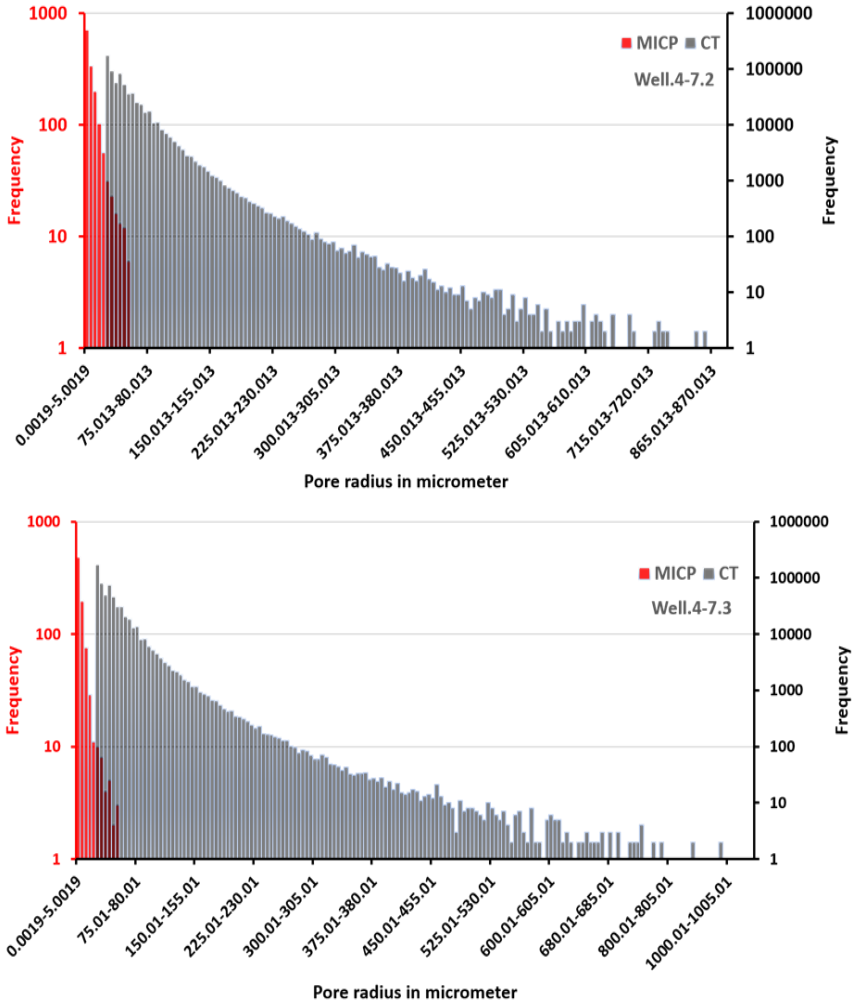


***Figure 12***

*Comparison of PSD measured by μ-CT analysis and MICP: PSD histogram by μ-CT analysis results and axis shown in black, MICP results and axis shown in red.*

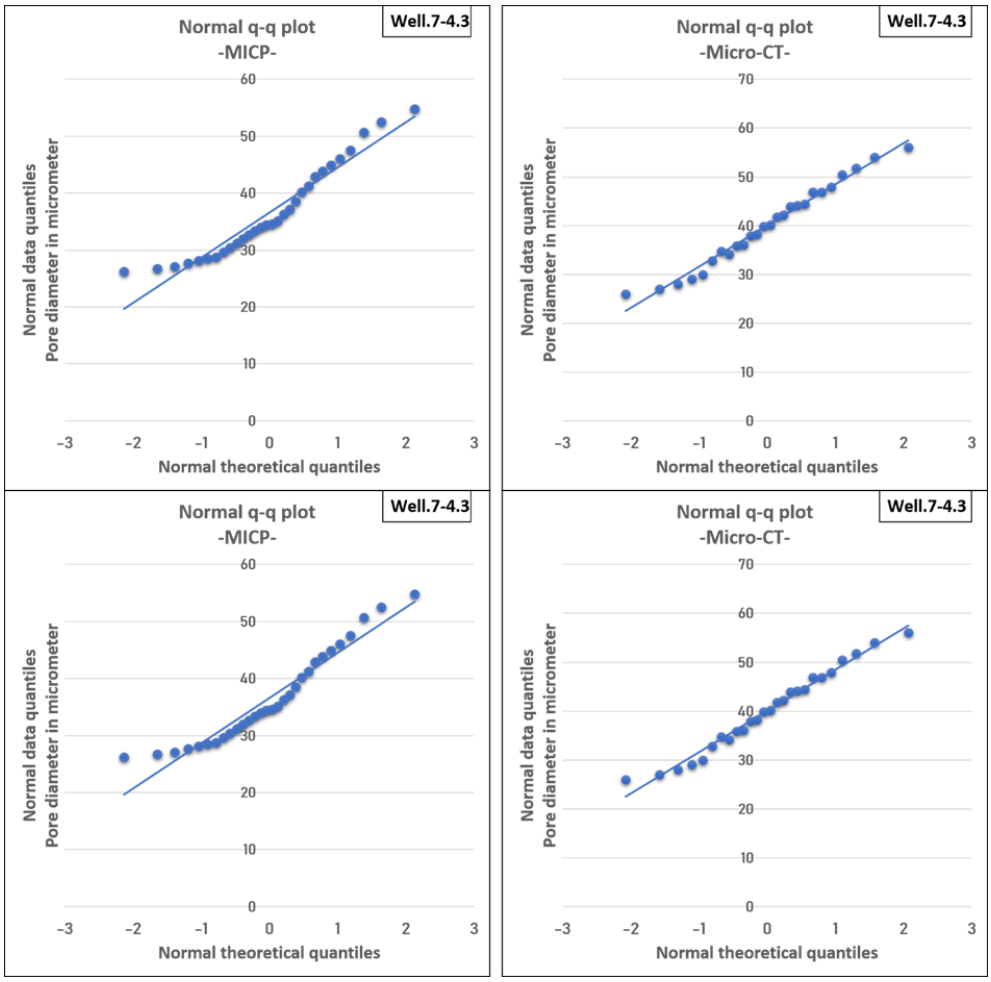


***Figure 13***

*Normal q-q plot for the overlapping interval in Figure 12, to demonstrate the similarity of CT-PSD and that measured by MICP. For all figures the pore diameter is on the vertical axis compared to standard normal population on the horizontal axis*

## 4. CONCLUSION

X-ray microtomography is at present one of the best and most modern research methods used by geologists and petrophysicists where material characterization plays important role. This method enables visualization of the internal structure of the rock, helping to understand the petrophysical properties of the reservoir rocks, and allowing the flow phenomena of different fluid reservoirs in the rock pore space to be simulated. This paper compared the results of micro-CT measurements with those of MICP measured in the lab.

Micro-CT analysis provides some useful information about the pore topology and structure as far as the the resolution is sufficient to capture the pore spaces of the sample. To resolve the limitation of this methodology, one suggestion is to scan a smaller plug and increase the volume size examined numerically by using discrete representations of the pore space at the relevant scale in dual pore networks or by using continuum type upscaling techniques to predict flow properties in multi scale heterogeneous samples [14]. Other approaches are to, improve the resolution of micro-CT-scanners, or to use advanced image registration techniques and kriging or similar procedures for better thresholding in order to better detect pore networks [15].

To conclude, further research should be undertaken in the evaluation of pore structure, where smaller plugs will be scanned in order to achieve better image resolution, suitable for subsequent quantitative geometrical analysis, and modeling of fluid distributions and flow processes in discretized porous media.

**ACKNOWLEDGEMENTS**

A.H. thanks for Stipendium Hungaricum provided by the Hungarian Government. MOL Hungary is thanked for providing the samples. Prof. Dr. Valéria Mertinger and Ádám Filep are thanked for providing the CT-scan for the samples.

**REFERENCES**

[1] Riepe, L., Suhaimi, M., Kumar, M., Knackstedt, M. (2011). Application of high-resolution micro-CT imaging and Pore Network Modeling (PNM) for the petrophysical characterization of tight gas reservoirs. A case history from a deep clastic tight gas reservoir in Oman. *Society of Petroleum Engineers – SPE Middle East Unconventional Gas Conference and Exhibition*, UGAS, 262–274, https://doi.org/10.2118/142472-ms.

[2] Wildenschild, D., Vaz, C., Rivers, M., Rikard, D., Christensen, B. (2002). Using X-ray computed tomography in hydrology: systems, resolutions, and limitations. *Journal of Hydrology*, 267, pp. 285–297.

[3] Cnudde, V., Boone, M. N. (2013). High-resolution X-ray computed tomography in geosciences: a review of the current technology and applications. *Earth Science Reviews*, 123, pp. 1–17, DOI:10.1016/j.earscirev. 2013.04.003.

[4] Ketcham, R.A., Carlson, W.D. (2001). Acquisition, optimization and interpretation of X-ray computed tomographic imagery: applications to the geosciences. *Computers & Geosciences*, 27 (4), pp. 381–400, DOI:10.1016/ S0098-3004(00)00116-3.

[5] Pullan, B. R., Ritchings, R. T., Isherwood, I. (1981). Accuracy and meaning of computed tomography attenuation values. In: Newton, T. H., Potts, D. G.

(eds.) *Radiology of the Skull and Brain. Technical Aspects of Computed Tomography.* 5, pp. 3904–3917.

[6] Claes, S., Van De Walle, W., Islahuddin, M., Janssen, H. (2020). The application of computed tomography for characterizing the pore structure of building materials. *Journal of Building Physics*, 43 (4), pp. 254–276, DOI:10. 1177/1744259119880927.

[7] Wildenschild, D., Sheppard, A. P. (2013). Advances in Water Resources X-ray imaging and analysis techniques for quantifying pore-scale structure and processes in subsurface porous medium systems. *Advances in Water Resources*, 51, pp. 217–246.

[8] Garnica, C., Boochs, F., Twardochlib, M. (2000). A new approach to edge-preserving smoothing for edge extraction and image segmentation, ISPRS Symposium, Amsterdam, The Netherlands. *International Archives of Photogrammetry and Remote Sensing*, Vol. XXXIII, Part B3, pp. 320–325.

[9] Kaestner, A., Lehmann, E., Stampanoni, M. (2008). Imaging and image processing in porous media research. *Advances in Water Resources*, 30, pp. 168–1178, DOI:10.1016/j.advwatres.2008.01.022.

[10] Weickert, J., Ter Haar Romeny, B. M., Viergever, M. (1998). Efficient and reliable schemes for nonlinear diffusion filtering. *IEEE Transactions on Image Processing*, 7 (3), pp. 398–410, https://doi.org/10.1109/83.661190.

[11] Pal, N. R., Pal, S. K. (1993). A review on image segmentation techniques. *Pattern Recognition*, 26, pp. 1277–1294. DOI:10.1016/0031-3203(93)90135-J.

[12] Sezgin, M., Sankur, B. (2004). Survey over image thresholding techniques and quantitative performance evaluation. *Journal of Electronic Imaging*, 13, pp. 146–165, DOI:10.1117/1.1631315.

[13] Mukhtar, T. (2020). *Sedimentological Control on the Productive and Dry Intervals in Four Investigated Wells.* Master Thesis, University of Miskolc.

[14] Youssef, S., Rosenberg, E., Gland, N., Bekri, S., Vizika, O. (2007). Quantitative 3D characterisation of the pore space of real rocks: improved μCT resolution and pore extraction methodology. In: *Proc. International Symposium of the Society of Core Analysts*, Calgary, Canada, September 10–12, pp. 1–13.

[15] Sarker, M. R. H., Siddiqui, S. (2009). Advances in micro-CT based evaluation of reservoir rocks. *Society of Petroleum Engineers – SPE Saudi Arabia Section Technical Symposium*, pp. 9–11, DOI:10.2118/126039-ms.